

PAPER • OPEN ACCESS

Overview of first Wendelstein 7-X high-performance operation





To cite this article: T. Klinger *et al* 2019 *Nucl. Fusion* **59** 112004

View the [article online](#) for updates and enhancements.

Recent citations

- [Verification of the global gyrokinetic stellarator code XGC-S for linear ion temperature gradient driven modes](#)
M. D. J. Cole *et al*
- [Plasma termination by excess pellet fuelling and impurity injection in TJ-II, the Large Helical Device and Wendelstein 7-X](#)
A. Dinklage *et al*
- [First divertor physics studies in Wendelstein 7-X](#)
T. Sunn Pedersen *et al*

Overview of first Wendelstein 7-X high-performance operation

T. Klinger^{1,2}, T. Andreeva¹, S. Bozhenkov¹ , C. Brandt¹, R. Burhenn¹, B. Buttenschön¹ , G. Fuchert¹, B. Geiger¹, O. Grulke^{1,3}, H.P. Laqua¹, N. Pablant⁴, K. Rahbarnia¹, T. Stange¹, A. von Stechow¹, N. Tamura⁵ , H. Thomsen¹, Y. Turkin¹, T. Wegner¹ , I. Abramovic¹, S. Äkäslompolo¹, J. Alcuson¹, P. Aleynikov¹, K. Aleynikova¹, A. Ali¹, A. Alonso⁶, G. Anda⁷, E. Ascasibar⁶, J.P. Böhner¹, S.G. Baek⁹, M. Balden¹⁰, J. Baldzuhn¹, M. Banduch¹, T. Barbui¹¹, W. Behr⁸, C. Beidler¹, A. Benndorf¹, C. Biedermann¹, W. Biel⁸, B. Blackwell¹², E. Blanco⁶, M. Blatzheim¹, S. Ballinger⁹, T. Bluhm¹, D. Böckenhoff¹, B. Böswirth¹⁰, L.-G. Böttger^{1,3}, M. Borchardt¹, V. Borsuk⁸, J. Boscary¹⁰, H.-S. Bosch¹, M. Beurskens¹, R. Brakel¹, H. Brand¹³, T. Bräuer¹, H. Braune¹, S. Brezinsek⁸, K.-J. Brunner¹, R. Bussiahn¹, V. Bykov¹, J. Cai⁸, I. Calvo⁶, B. Cannas¹⁴, A. Cappa⁶, A. Carls¹, D. Carralero⁶, L. Carraro¹⁵, B. Carvalho¹⁶, F. Castejon⁶, A. Charl⁸, N. Chaudhary¹, D. Chauvin¹⁷, F. Chernyshev¹⁸, M. Cianciosa¹⁹, R. Citarella²⁰, G. Claps²¹, J. Coenen⁸, M. Cole¹, M.J. Cole¹⁹, F. Cordella²¹, G. Cseh⁷, A. Czarnecka²², K. Czerski²³, M. Czerwinski¹, G. Czymek⁸, A. da Molin²⁴, A. da Silva¹⁷, H. Damm¹, A. de la Pena⁶, S. Degenkolbe¹, C.P. Dhard¹, M. Dibon¹⁰, A. Dinklage¹, T. Dittmar⁸, M. Drevlak¹, P. Drewelow¹, P. Drews⁸, F. Durodie²⁶, E. Edlund⁹, P. van Eeten¹, F. Effenberg¹¹, G. Ehrke¹, S. Elgeti¹⁰, M. Endler¹, D. Ennis²⁷, H. Esteban⁶, T. Estrada⁶, J. Fellinger¹, Y. Feng¹, E. Flom¹¹, H. Fernandes¹⁷, W.H. Fietz²⁵, W. Figacz²², J. Fontdecaba⁶, O. Ford¹, T. Fornal²², H. Frerichs¹⁰, A. Freund⁸, T. Funaba⁵, A. Galkowski²², G. Gantenbein²⁵, Y. Gao⁸, J. García Regaña⁶, D. Gates⁴, J. Geiger¹, V. Giannella²⁰, A. Gogoleva²⁸, B. Goncalves¹⁷, A. Gorlaev²⁶, D. Gradic¹, M. Grahl¹, J. Green¹¹, H. Greuner¹⁰, A. Grosman¹⁷, H. Grote¹, M. Gruca²², C. Guerard⁶, P. Hacker¹, X. Han⁸, J.H. Harris¹⁹, D. Hartmann¹, D. Hathiramani¹, B. Hein¹, B. Heinemann¹⁰, P. Helander^{1,2}, S. Henneberg¹, M. Henkel⁸, J. Hernandez Sanchez⁶, C. Hidalgo⁶, M. Hirsch¹, K.P. Hollfeld⁸, U. Höfel¹, A. Hölting¹, D. Höschen⁸, M. Houry¹⁷, J. Howard¹³, X. Huang⁵, Z. Huang¹, M. Hubeny⁸, M. Huber²⁵, H. Hunger²⁵, K. Ida⁵, T. Ilkei⁷, S. Illy²⁵, B. Israeli⁴, S. Jablonski²², M. Jakubowski¹, J. Jelonnek²⁵, H. Jenzsch¹, T. Jesche²⁹, M. Jia⁸, P. Junghanns¹⁰, J. Kacmarczyk²², J.-P. Kallmeyer¹, U. Kamionka¹, H. Kasahara⁵, W. Kasperek²⁹, Y.O. Kazakov²⁶, N. Kenmochi⁵, C. Killer¹, A. Kirschner⁸, R. Kleiber¹, J. Knauer¹, M. Knaup⁸, A. Knieps⁸, T. Kobarg²⁵, G. Kocsis⁷, F. Köchl³⁰, Y. Kolesnichenko³¹, A. Könies¹, R. König¹, P. Kornejew¹, J.-P. Koschinsky¹, F. Köster³², M. Krämer²⁹, R. Krampitz¹, A. Krämer-Flecken⁸, N. Krawczyk²², T. Kremeyer¹¹, J. Krom¹, M. Krychowiak¹, I. Ksiązek³³, M. Kubkowska²², G. Kühner¹, T. Kurki-Suonio³⁴, P.A. Kurz¹, S. Kwak¹, M. Landreman³⁵, P. Lang¹⁰, R. Lang²⁵, A. Langenberg¹,



Original content from this work may be used under the terms of the [Creative Commons Attribution 3.0 licence](https://creativecommons.org/licenses/by/3.0/). Any further distribution of this work must maintain attribution to the author(s) and the title of the work, journal citation and DOI.

S. Langish⁴, H. Laqua¹, R. Laube¹, S. Lazerson⁴, C. Lechte²⁹, M. Lennartz⁸, W. Leonhardt²⁵, C. Li¹, C. Li⁸, Y. Li⁸, Y. Liang⁸, C. Linsmeier⁸, S. Liu⁸, J.-F. Lobsien¹, D. Loesser⁶, J. Loizu Cisquella¹, J. Lore¹⁹, A. Lorenz¹, M. Losert²⁵, A. Lücke, A. Lumsdaine¹⁹, V. Lutsenko³¹, H. Maaßberg¹, O. Marchuk⁸, J.H. Matthew¹², S. Marsen¹, M. Marushchenko¹, S. Masuzaki⁵, D. Maurer²⁷, M. Mayer¹⁰, K. McCarthy⁶, P. McNeely¹, A. Meier²⁵, D. Mellein²⁵, B. Mendeleevitch¹⁰, P. Mertens⁸, D. Mikkelsen⁴, A. Mishchenko¹, B. Missal¹, J. Mittelstaedt⁴, T. Mizuuchi, A. Mollen¹, V. Moncada¹⁷, T. Mönnich¹, T. Morisaki⁵, D. Moseev¹, S. Murakami, G. Náfrádi⁷, M. Nagel¹, D. Naujoks¹, H. Neilson⁴, R. Neu¹⁰, O. Neubauer⁸, U. Neuner¹, T. Ngo¹⁷, D. Nicolai⁸, S.K. Nielsen³, H. Niemann¹, T. Nishizawa¹, R. Nocentini¹⁰, C. Nührenberg¹, J. Nührenberg¹, S. Obermayer¹⁰, G. Offermanns⁸, K. Ogawa⁵, J. Ölmanns⁸, J. Ongena²⁶, J.W. Oosterbeek¹, G. Orozco¹⁰, M. Otte¹, L. Pacios Rodriguez⁶, N. Panadero¹, N. Panadero Alvarez⁶, D. Papenfuß²⁵, S. Paqay¹³, E. Pasch¹, A. Pavone¹, E. Pawelec³³, T.S. Pedersen^{1,2}, G. Pelka²², V. Perseo¹, B. Peterson⁵, D. Pilopp¹, S. Pingel¹, F. Pisano¹⁴, B. Plaum²⁹, G. Plunk¹, P. Pölöskei¹⁰, M. Porkolab⁹, J. Proll¹³, M.-E. Puiatti³⁶, A. Puig Sitjes¹, F. Purps¹, M. Rack⁸, S. Récséi⁷, A. Reiman⁴, F. Reimold¹, D. Reiter⁸, F. Remppel²⁹, S. Renard¹⁷, R. Riedl¹⁰, J. Riemann¹, K. Risse¹, V. Rohde¹⁰, H. Röhlinger²⁹, M. Romé³⁶, D. Rondeshagen¹, P. Rong¹, B. Roth²⁹, L. Rudischhauser¹, K. Rummel¹, T. Rummel¹, A. Runov¹, N. Rust¹, L. Ryc²², S. Ryosuke⁵, R. Sakamoto⁵, M. Salewski³, A. Samartsev²⁵, E. Sanchez⁶, F. Sano³⁷, S. Satake⁵, J. Schacht¹, G. Satheeswaran⁸, F. Schauer¹, T. Scherer²⁵, J. Schilling¹, A. Schlaich²⁵, G. Schlisio¹, F. Schluck⁸, K.-H. Schlüter²⁹, J. Schmitt²⁷, H. Schmitz⁸, O. Schmitz¹⁰, S. Schmuck³⁸, M. Schneider¹, W. Schneider¹, P. Scholz¹, R. Schrittwieser³⁰, M. Schröder¹, T. Schröder¹, R. Schroeder¹, H. Schumacher³⁹, B. Schweer²⁶, E. Scott¹, S. Sereda⁸, B. Shanahan¹, M. Sibilia⁴, P. Sinha¹, S. Sipliä³⁴, C. Slaby¹, M. Slecza²³, H. Smith¹, W. Spiess²⁵, D.A. Spong¹⁹, A. Spring¹, R. Stadler¹⁰, M. Stejner³, L. Stephey¹¹, U. Stridde¹, C. Suzuki⁵, J. Svensson¹, V. Szabó⁷, T. Szabolics⁷, T. Szepesi⁷, Z. Szökefalvi-Nagy⁷, A. Tancetti³, J. Terry⁹, J. Thomas⁸, M. Thumm²⁵, J.M. Travers¹⁷, P. Traverso²⁷, J. Tretter¹⁰, H. Trimino Mora¹, H. Tsuchiya⁵, T. Tsujimura⁵, S. Tulipán⁷, B. Unterberg⁸, I. Vakulchik¹, S. Valet¹, L. Vano⁷, B. van Milligen⁶, A. J. van Vuuren¹⁰, L. Vela²⁸, J.-L. Velasco⁶, M. Vergote²⁶, M. Vervier²⁶, N. Vianello¹⁵, H. Viebke¹, R. Vilbrandt¹, A. Vorköper¹, S. Wadle²⁵, F. Wagner¹, E. Wang⁸, N. Wang⁸, Z. Wang¹, F. Warmer¹, T. Wauters²⁶, L. Wegener¹, J. Weggen²⁵, Y. Wei⁸, G. Weir¹, J. Wendorf¹, U. Wenzel¹, A. Werner¹, A. White⁹, B. Wiegel⁹, F. Wilde¹, T. Windisch¹, M. Winkler¹, A. Winter¹, V. Winters¹¹, S. Wolf²⁹, R.C. Wolf^{1,32}, A. Wright¹², G. Wurden⁴⁰, P. Xanthopoulos¹, H. Yamada⁵, I. Yamada⁵, R. Yasuhara⁵, M. Yokoyama⁵, M. Zanini¹, M. Zarnstorff⁴, A. Zeitler²⁹, D. Zhang¹, H. Zhang⁶, J. Zhu¹, M. Zilker¹⁰, A. Zocco¹, S. Zoletnik⁷ and M. Zuin¹³

¹ Max-Planck Institute for Plasma Physics, Wendelsteinstrasse 1, 17491 Greifswald, Germany

² Greifswald University, Domstrasse 11, 17489 Greifswald, Germany

³ Technical University of Denmark, Anker Engelunds Vej 1, 2800 Kgs. Lyngby, Denmark

⁴ Princeton Plasma Physics Laboratory, 100 Stellarator Rd, Princeton, NJ 08540, United States of America

⁵ National Institute for Fusion Science, 322-6 Oroshicho, Toki, Gifu Prefecture 509-5202, Japan

⁶ CIEMAT, Avenida Complutense, 40, 28040 Madrid, Spain

⁷ Wigner Research Centre for Physics, Konkoly Thege Miklos ut 29-33, 1121 Budapest, Hungary

⁸ Research Center Jülich GmbH, Institute for Energy and Climate Research Plasma Physics, Wilhelm-Johnen-Strasse, 52428 Jülich, Germany

- ⁹ Massachusetts Institute of Technology, 77 Massachusetts Ave, Cambridge, MA 02139, United States of America
- ¹⁰ Max-Planck Institute for Plasma Physics, Boltzmannstrasse 2, 85748 Garching, Germany
- ¹¹ University of Wisconsin Madison, Engineering Drive, Madison, WI 53706, United States of America
- ¹² The Australian National University, Acton ACT 2601, Canberra, Australia
- ¹³ Eindhoven University of Technology, 5612 AZ Eindhoven, Netherlands
- ¹⁴ University of Cagliari, Via Università, 40, 09124 Cagliari, Italy
- ¹⁵ Consorzio RFX, Corso Stati Uniti, 4-35127 Padova, Italy
- ¹⁶ Instituto de Plasmas e Fusão Nuclear, Av. Rovisco Pais, 1049-001 Lisboa, Portugal
- ¹⁷ CEA Cadarache, 13115 Saint-Paul-lez-Durance, France
- ¹⁸ Ioffe Physical-Technical Institute of the Russian Academy of Sciences, 26 Politekhnicheskaya, St Petersburg 194021, Russian Federation
- ¹⁹ Oak Ridge National Laboratory, 1 Bethel Valley Rd, Oak Ridge, TN 37830, United States of America
- ²⁰ University of Salerno, Via Giovanni Paolo II, 132, 84084 Fisciano SA, Italy
- ²¹ ENEA Centro Ricerche Frascati, Via Enrico Fermi, 45, 00044 Frascati RM, Italy
- ²² Institute of Plasma Physics and Laser Microfusion, 23 Hery Str., 01-497 Warsaw, Poland
- ²³ University of Szczecin, 70-453, aleja Papiea Jana Pawa II 22A, Szczecin, Poland
- ²⁴ University of Milano-Bicocca, Piazza dell'Ateneo Nuovo, 1-20126, Milano, Italy
- ²⁵ Karlsruhe Institute of Technology, Hermann-von-Helmholtz-Platz 1, 76344 Eggenstein-Leopoldshafen, Germany
- ²⁶ Royal Military Academy, Avenue de la Renaissance 30, B-1000 Brussels, Belgium
- ²⁷ Auburn University, Auburn, AL 36849, United States of America
- ²⁸ Universidad Carlos III de Madrid, Av. de la Universidad, 30, Madrid, Spain
- ²⁹ Institute for Surface Process Engineering and Plasma Technology, University of Stuttgart, Nobelstrasse 12, 70569 Stuttgart, Germany
- ³⁰ Austrian Academy of Science, Doktor-Ignaz-Seipel-Platz 2, 1010 Wien, Austria
- ³¹ Institute for Nuclear Research, b.47, prospekt Nauky, Kiev 03680, Ukraine
- ³² Technical University of Berlin, Strasse des 17. Juni 135, 10623 Berlin, Germany
- ³³ University of Opole, plac Kopernika 11a, 45-001 Opole, Poland
- ³⁴ Aalto University, 02150 Espoo, Finland
- ³⁵ University of Maryland, Paint Branch Drive, College Park, MA 20742, United States of America
- ³⁶ Istituto di Fisica del Plasma Piero Caldirola, Via Roberto Cozzi, 53, 20125 Milano, Italy
- ³⁷ Kyoto University, Yoshidahonmachi, Sakyo Ward, Kyoto, Kyoto Prefecture 606-8501, Japan
- ³⁸ Culham Centre for Fusion Energy, Abingdon OX14 3EB, United Kingdom
- ³⁹ Physikalisch Technische Bundesanstalt (PTB), Bundesallee 100, 38116 Braunschweig, Germany
- ⁴⁰ Los Alamos National Laboratory, Los Alamos, NM 87544, United States of America

E-mail: thomas.klinger@ipp.mpg.de

Received 23 November 2018, revised 15 January 2019

Accepted for publication 31 January 2019

Published 5 June 2019



Abstract

The optimized superconducting stellarator device Wendelstein 7-X (with major radius $R = 5.5$ m, minor radius $a = 0.5$ m, and 30 m³ plasma volume) restarted operation after the assembly of a graphite heat shield and 10 inertially cooled island divertor modules. This paper reports on the results from the first high-performance plasma operation. Glow discharge conditioning and ECRH conditioning discharges in helium turned out to be important for density and edge radiation control. Plasma densities of $1\text{--}4.5 \times 10^{19}$ m⁻³ with central electron temperatures $5\text{--}10$ keV were routinely achieved with hydrogen gas fueling, frequently terminated by a radiative collapse. In a first stage, plasma densities up to 1.4×10^{20} m⁻³ were reached with hydrogen pellet injection and helium gas fueling. Here, the ions are indirectly heated, and at a central density of $8 \cdot 10^{19}$ m⁻³ a temperature of 3.4 keV with $T_e/T_i = 1$ was transiently accomplished, which corresponds to $nT_i(0)\tau_E = 6.4 \times 10^{19}$ keV s m⁻³ with a peak diamagnetic energy of 1.1 MJ and volume-averaged normalized plasma pressure $\langle\beta\rangle = 1.2\%$. The routine access to high plasma densities was opened with boronization of the first wall. After boronization, the oxygen impurity content was reduced by a factor of 10, the carbon impurity content by a factor of 5. The reduced (edge) plasma radiation level gives routinely access to higher densities without radiation collapse, e.g. well above 1×10^{20} m⁻² line integrated density and $T_e = T_i = 2$ keV central temperatures at moderate ECRH power. Both

X2 and O2 mode ECRH schemes were successfully applied. Core turbulence was measured with a phase contrast imaging diagnostic and suppression of turbulence during pellet injection was observed.

Keywords: stellarator, divertor, ECR heating, NBI heating, plasma performance, turbulence, impurities

(Some figures may appear in colour only in the online journal)

1. Introduction

Stellarators are free from current disruptions and are intrinsically capable to sustain a plasma steady-state without need for current drive [1]. The stellarator magnetic field, however, needs to be optimized to overcome major issues in neoclassical transport, magnetohydrodynamic equilibrium and stability, and fast particle confinement, in particular at high plasma beta and low collisionality [2–4]. After successful first operation [5–7], the optimized stellarator device Wendelstein 7-X [8,9] is now operating with (yet uncooled) graphite heat shields and a graphite island divertor [10, 11]. Wendelstein 7-X is a high- ι , low shear stellarator with optimized magnetic field geometry and 30 m³ plasma volume. It is the mission of the device to demonstrate steady-state (pulse length $T_p \leq 1800$ s) generation and confinement of fusion-relevant hydrogen and deuterium plasmas. The magnetic field with induction 2.5 T on the magnetic axis is generated using a set of non-planar and planar liquid-helium cooled superconducting NbTi coils. All plasma facing components are designed for active water cooling capability. Steady-state electron cyclotron resonance plasma heating is provided by long-pulse gyrotrons. Neutral beam injectors and ion cyclotron resonance heating are foreseen for high beta plasmas and fast particle physics investigations.

The device operation phase reported in the present paper is performed without water cooling of the main in-vessel components. This restricts the heating energy input to 200 MJ. High-performance plasma operation is nevertheless possible, but at limited pulse lengths (typical 10–30 s). Long discharges (up to 100 s) are restricted to lower heating power and consequently lower plasma performance. Fully integrated divertor operation must be demonstrated to develop a basis for high-performance steady-state operation which follows after the completion of the cooling water systems and the installation of the water-cooled divertor and the cryo pumps.

The present paper is structured in a machine description section 2, long-pulse high density plasmas section 3, and stellarator optimization section 4. The paper is summarized in section 5.

2. The Wendelstein 7-X stellarator device

As pointed out in section 1, the magnetic field geometry of the superconducting stellarator Wendelstein 7-X was optimized to address major issues of the classical stellarator [3, 4]. A schematic drawing of the device and the rotational transform

of some of the magnetic field configurations are shown in figure 1. The 50 non-planar coils (red) and 20 planar coils (orange) are connected in series via superconducting bus bars. All coils are bolted to a massive central support ring (gray) and additionally fixed by mostly welded, partially bolted or sliding local support elements. The complete magnet system and the support structures are cooled down to 3.4 K in the cryostat vacuum between the outer vessel and the plasma vessel. Both the plasma vessel, the outer vessel and the 253 ports are covered with a thermal insulation, based on multi-layer foil and a thermal shield actively cooled to 70 K [12].

The main device parameters are listed in table 1. Stage 1 was the setup for the initial operation. After substantial extension of the in-vessel components and the heating systems, the present stage 2 was reached. Stage 3 is planned for the subsequent operation phase. Stage 4 is the projected full performance configuration of the device. The most powerful heating scheme of Wendelstein 7-X is the electron cyclotron resonance heating (ECRH) with at present 10 long-pulse capable 140 GHz gyrotrons [13]. On average each gyrotron accounts for 0.8 MW power coupled into the plasma which provides a highly flexible X2-mode and O2-mode heating scheme, both on- and off-axis. The flexibility and the well-defined heat deposition in the electron cyclotron resonance zone render ECRH being the most advanced heating and current drive scheme with the biggest potential for a future stellarator power reactor [14]. The first of two neutral beam injector (NBI) boxes have started operation with two positive ion sources and 55 kV acceleration voltage and up to 3.5 MW injection power [15]. The ion cyclotron resonance heating (ICRH) system requires an antenna that is carefully shaped to the three-dimensional plasma contour. This development is ongoing and commissioning is foreseen for the next operation phase [16]. To protect the (mostly uncooled) in-vessel components, the maximum heating energy during stage 2 is at present limited to 200 MJ, which implies typical discharge times between 10 and 100 s, depending on the input power. After completion of the water cooling systems and the replacement of the inertially cooled island divertor with an actively water-cooled one, the maximum heating energy will be extended step-wise to 18 GJ with at least one intermediate step at 1 GJ (stage 3).

Wendelstein 7-X started first operation in the year 2015. The heat and particle exhaust was controlled with five poloidal graphite limiters, the remaining wall was either steel or CuCrZr. Despite the unfavorable wall conditions, the plasma performance was quite remarkable with peak electron temperatures 8 keV with simultaneous peak ion temperature

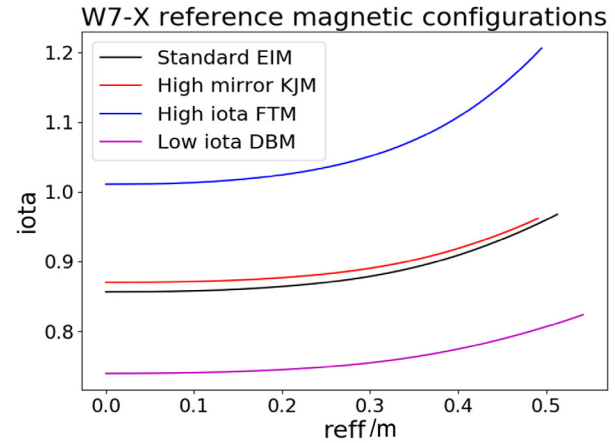
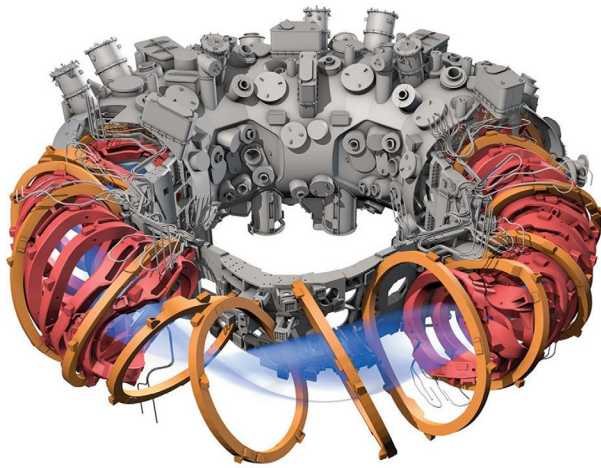


Figure 1. Schematic diagram of the superconducting stellarator device Wendelstein 7-X. The last closed magnetic flux surface is indicated in light blue. The 50 non-planar (red) and the 20 planar (orange) superconducting coils are operated in a evacuated cryostat volume between the plasma vessel and the outer vessel. Wendelstein 7-X is a high-iota low-shear device and the iota profiles ($\beta = 0$) of some reference magnetic configurations are shown on the right hand side. The reference configurations are standard (EIM), high mirror ratio (KJM), high iota (FTM), and low iota (DBM).

2 keV and line averaged density $3 \times 10^{19} \text{ m}^{-3}$ [5–7]. These are typical conditions for the core electron root confinement [5–7, 17] which is characterized by a reversal of the radial electric field from edge to core [18]. First elements of stellarator optimization could be demonstrated by studying the bootstrap current and neoclassical transport [19].

For the second operation phase (stage 2) the limiters were replaced by an island divertor and major areas of the wall are covered with graphite tiles. The island divertor consists of ten separate modules formed by graphite target and baffle plates that are matched to the magnetic field structure of Wendelstein 7-X [10, 11]. Depending on the magnetic configuration (given by the rotational transform $\iota/2\pi$, see figure 1) natural magnetic islands form at the plasma boundary. They are intersected with the divertor target plates and thus establish a multi-X-point divertor for the exhaust of particle and heat flows across the last closed flux surface. The aim of the second operation phase is to demonstrate full divertor operation and exhaust combined with improved plasma performance.

3. High density stationary discharges

The plasma performance of Wendelstein 7-X in terms of plasma density, ion temperature, stored energy, and discharge duration has dramatically improved after the installation of the graphite heat shields and the graphite island divertor. Another significant step forward was made with a suite of wall conditioning measures [20]: The plasma vessel is baked at 150 °C in order to remove water and hydrocarbons from the vessel wall and in-vessel components. Without magnetic field, glow discharge cleaning (GDC) is applied in hydrogen (to reduce residual CO and CH₄) and helium gas (to reduce H₂). With the superconducting magnets ramped up, an additional wall conditioning inbetween discharges was made with ECRH short pulse trains followed by pumping intervals. The GDC in helium and hydrogen as well as the occasional ECRH pulse train conditioning of the plasma facing

Table 1. Major parameters of the stellarator Wendelstein 7-X. The different stages of completion and extension mainly determine the available heating power and the active cooling of the in-vessel components.

Quantity	Unit	Stage 1	Stage 2	Stage 3	Stage 4
Plasma volume	m ³			30	
Major radius	m			5.5	
Minor radius	m			0.5	
Magnetic induction on axis	T			2.5	
Rotational transform	2π			5/6...5/4	
ECR heating power	MW	4.3	8.5	10	10–15
ICR heating power	MW			1.5	3.5
NBI heating power H/D	MW		3.5	7/10	14/20
Heating energy	MJ	4	200	1000	18000
Pulse length typ.	s	1–2	10–100	100–200	100–1800

components (with total surface areas of 88 m² graphite and 82 m² steel) have greatly reduced the outgassing rates, rapidly dropping to values that were reached only at the end of the initial (stage 1) operation phase with graphite limiters. Plasma densities of $1\text{--}5 \times 10^{19} \text{ m}^{-3}$ with electron temperature 5–10 keV were achieved with hydrogen gas fueling; higher densities were not accessible due to the radiative limit. High plasma densities up to $1.4 \times 10^{20} \text{ m}^{-3}$ could be reached with repetitive hydrogen pellet injection and second harmonic ECR heating in O-polarization (O2-scheme, see figure 3(b) below). In a similar scenario with hydrogen plasma, at a central density of $8 \times 10^{19} \text{ m}^{-3}$, the ions are indirectly heated and a temperature of 3.4 keV with $T_e/T_i \approx 1$ was accomplished, still with second harmonic ECR heating in X-polarization (X2-scheme). This discharge corresponds to a (stellarator) record $nT_i(0)\tau_E = 6.4 \times 10^{19} \text{ keV s m}^{-3}$ with

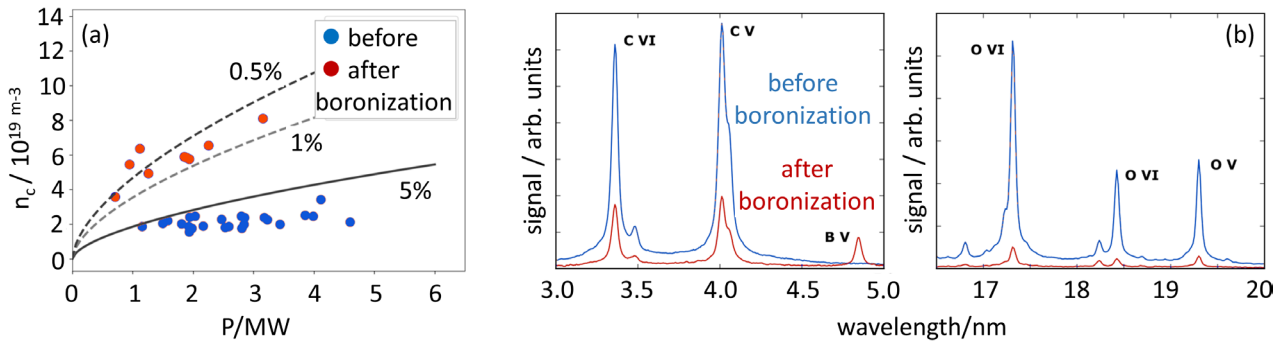


Figure 2. (a) Maximum density achieved before onset of radiation collapse versus heating power before (blue symbols) and after boronization (red symbols). The lines indicate the predicted critical density n_c for different impurity fractions $f_{\text{imp}} = 5\%$, 1% and 0.5% . (b) Spectral lines of C and O ionization stages before and after boronization. At about 4.9 nm a small B V line arises after boronization.

a peak diamagnetic energy of 1.1 MJ and volume-averaged normalized plasma pressure $\langle\beta\rangle = 1.5\%$ [21, 22]. The corresponding radial temperature and density profiles are both centrally peaked with typical gradient lengths $L_{T_e} \approx 3\text{--}4$ m and $L_n \approx 2\text{--}3$ m. The radial density profile significantly steepens with central fueling, e.g. by pellet injection or neutral beam injection (see below). Further details about the kinetic profiles are found in [21]. Routinely, stable 25 s long-pulse helium discharges with 2–3 MW ECRH power and up to 75 MJ injected energy were created for equilibrium and divertor load studies, with plasma densities around $5 \times 10^{19} \text{ m}^{-3}$ and 5 keV electron temperature.

Boronization was conducted for the first time half-way the experimental campaign [23] (in total three times). Here, a glow discharge with 10% diborane B_2H_6 in 90% helium background gas was operated for 4–5 h to deposit a boron layer of about 50–100 nm thickness. The boron layer turned out to last for at about 200 plasma seconds on the strike line position of the divertor targets and for at least about 2000 plasma seconds on other wall elements. In fact, the excellent wall conditions did not degrade significantly during the accumulated 2400 s of plasma duration between each two boronization cycles and it can be assumed that longer cycle times are well possible. Figure 2(a) shows the difference between the discharge conditions before and after boronization [24]. With the same ECR heating power and normal gas puffing, about $\times 3$ higher plasma densities could be reached without radiative collapse. This improvement is due to a reduced O and C content, which strongly reduces the radiative power losses predominantly in the plasma edge, where the radiative collapse usually starts. The observed critical densities and their scaling with heating power is compared to the scaling law derived in [25]. For the Wendelstein 7-X parameters the scaling $\bar{n}_c \propto P^{0.6}/f_{\text{imp}}^{0.4}$ is plotted for different impurity fraction values $f_{\text{imp}} = n_{\text{imp}}/n_e = 5\%$, 1% and 0.5% , respectively. Before boronization the observed n_c values scale weaker than predicted even for $f_{\text{imp}} = 5\%$. After boronization, there is a good agreement with the scaling law for $f_{\text{imp}} = 0.5\text{--}1\%$. To highlight the effect of boronization on O and C impurities, spectroscopic measurements of O V and O VI as well as C V and C VI ions before and after boronization are shown in figure 2(b). The spectroscopic signals are normalized to the line-averaged plasma density measured for the respective

discharge. Note that for the lower wavelengths, no absolute calibration is available and temperature and profile effects have not yet been taken into account. Nevertheless, a strong reduction of the spectral line strength by $\times 2.5$ for carbon and $\times 6.5 \dots 8$ for oxygen is evident and a similar reduction in the associated impurity concentration can be assumed. This is a clear indication for the expected gettering effect by the boron layer on the plasma facing components [26].

With the extension of the density limit, ECR heating schemes beyond the X-mode cut-off density $1.2 \times 10^{20} \text{ m}^{-3}$ became important. In O-mode polarization ECR waves have a cut-off density of $2.4 \times 10^{20} \text{ m}^{-3}$, with the drawback of relatively low absorption rate of 70%, even at the favorable high electron temperature $T_e \simeq 3$ keV and density $n_e = 1 \times 10^{20} \text{ m}^{-3}$. In combination with pellet injection, the heating scenario shown in figure 3 was developed [27–29]: The plasma start-up (here in helium) is made with three gyrotrons in X-mode polarization. During the following 2 s the polarization is changed to O-mode polarization. At $t = 2$ s the density ramp-up is steepened by repetitive hydrogen ice pellet injection and at $t = 3$ s further six gyrotrons (in O-mode) are added. At the peak density of $1.4 \times 10^{20} \text{ m}^{-3}$ the electron temperature is still close to 3 keV. The 141 GHz electron cyclotron emission (ECE) signal vanishes due to excess of the X2-mode cut-off density (indicated by the orange strip). The stray radiation signal always remains in an acceptable range, even in the device module where the wave launcher is located. In the optimum O2-heating regime, the stray radiation level is found to be below 10 kW m^{-2} .

As outlined above, wall boronization has greatly extended the plasma density range to much higher values. After the first successful experiments in helium plasmas combined with hydrogen pellet injection, the previously described ECR O2-heating scheme became also the reference heating scheme for high density gas fueled hydrogen plasmas as well [27–29]. An example is shown in figure 4. The ECR heating power is 6 MW in total and is almost fully absorbed. The radiation fraction stays constant at 60%. At the (line-integrated) plasma densities $> 1 \times 10^{20} \text{ m}^{-3}$ ions are efficiently heated by the electrons and one obtains almost thermal equilibration $T_e \approx T_i$. The divertor is fully detached [30] and the power load drops to ≤ 1.5 MW. The discharge duration was limited to 14 s due to the technical limit of 80 MJ maximum injected energy

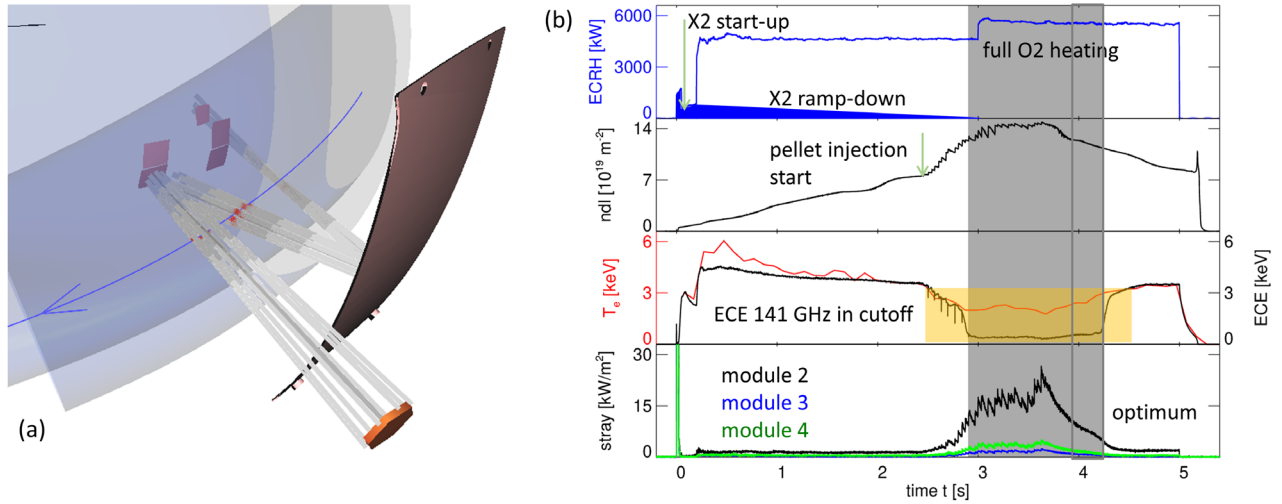


Figure 3. (a) Multi-pass absorption scheme using tungsten reflector tiles with holographic grating, mounted on the inner and the outer sides of the in-vessel system. (b) O2-mode heating scenario showing from top to bottom the heating power in X- and O-mode polarization (blue), the line-integrated density, the electron density measured by Thomson scattering (red) and electron cyclotron emission (black), and stray radiation measured in the device module where the wave launcher is located (black) and in the two neighboring modules (green and blue).

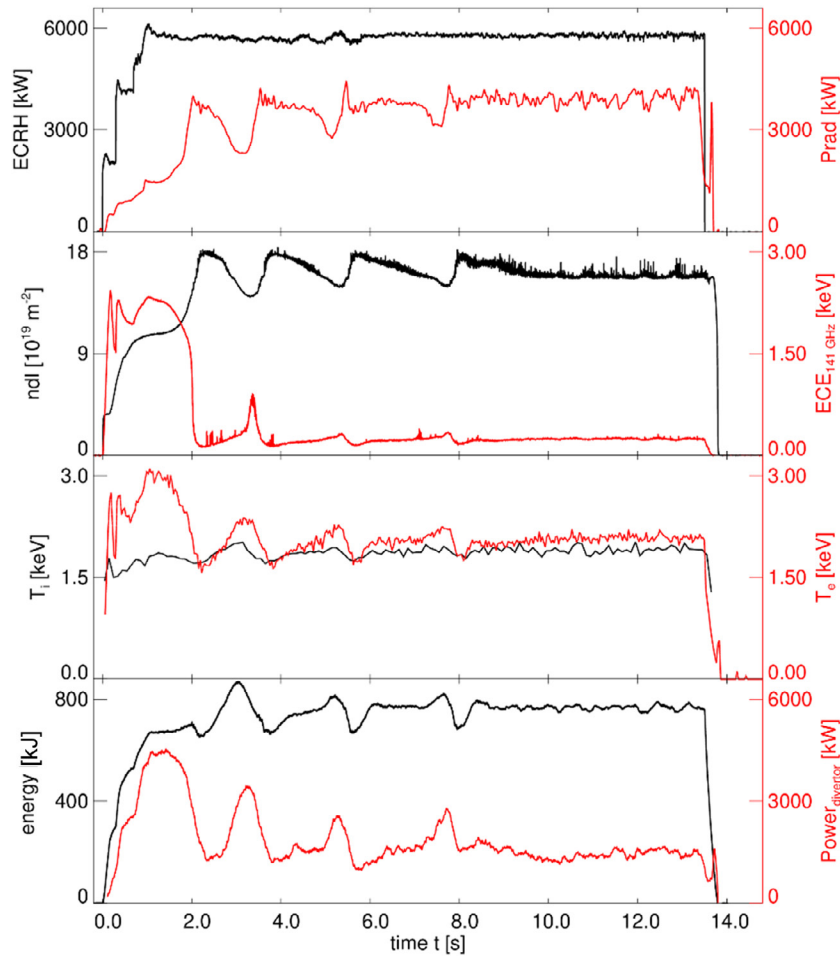


Figure 4. O2-mode heated long pulse high density plasma discharge. Shown are (from top to bottom, left and right scale) heating power, total radiative power, line-integrated density, electron cyclotron emission at 141 GHz, ion and electron temperature, diamagnetic energy and total divertor power load. The slow oscillations are generated by the feedback-controller. The 141GHz ECE channel runs into the cut-off after 2 s verifying the pure 140 GHz O2-heating.

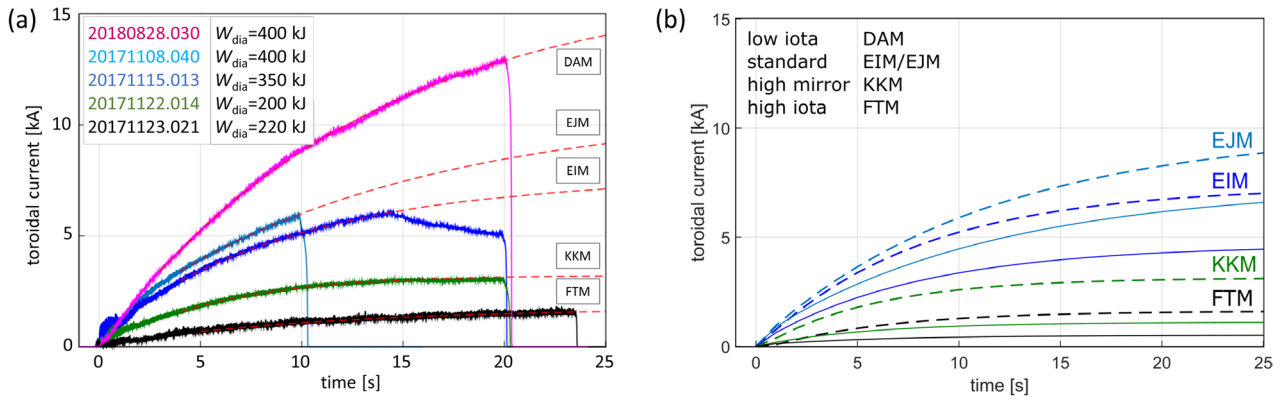


Figure 5. (a) Time evolution of the toroidal current measured with Rogowski coils. The different colors indicate the different magnetic configurations (see text). The dashed lines are exponential best-fits to the decaying shielding current. (b) Transport code simulations of the toroidal current based on experimental density and temperature profiles for the same magnetic configurations. Solid or dashed lines indicate simulation results without or with (unintended) residual ECCD, respectively: EJM 2.6 kA, EIM 2.7 kA, KKM 2.1 kA, FTM 1.8 kA.

set at that time period of operation. Since the divertor power detachment turned out to be well under control and the power load on the targets correspondingly low, the technical limit for the total heating energy could be extended from 80 to 200 MJ. A similar O₂-heated discharge could be extended to 30 s discharge duration at 5 MW heating power, again with full power detachment and similar plasma parameters [27]. In addition, high density operation could be demonstrated with pure neutral beam injection heating (3.5 MW H^+) after starting the plasma with ECRH (X2-mode). Possibly explained by the additional central fulling from the neutral beam, the plasma density increases throughout the NBI phase with more peaked density profiles and up to $n(0) = 2 \times 10^{20} \text{ m}^{-3}$. The ion temperature raises by about 10% to above 2 keV, the electron temperature drops after termination of the ECRH to values $\approx 20\%$ below T_i . The orbit losses related to the neutral beam injection are discussed in [27].

4. Stellarator optimization

It is the ultimate goal of Wendelstein 7-X to demonstrate the beneficial effect of the optimized magnetic field geometry, in particular reduced neoclassical transport and bootstrap current along with magnetic islands well-localized at the edge and good magneto-hydrodynamic stability [4]. Fast particle confinement is another important aspect of optimization [31]. The sum of all should result in improved plasma confinement and fully integrated, stable plasma scenarios with simultaneously high $T_i \approx T_e$ at high particle densities. In the ion root regime [32], the energy confinement times τ_E are expected to be better than the ISS04 [33] stellarator scaling if most of the energy transport is neoclassical. High-performance plasma scenarios require good control of the plasma-wall interaction (in particular the impurity source), the heat and particle exhaust as well as the particle recycling. Details are discussed in [30]. In this section we present a number of experimental results that provide evidence for successful stellarator optimization.

Figure 5(a) shows Rogowski coil measurements of the time evolution of the net toroidal plasma current for plasmas

with constant ECR heating power in different magnetic field configurations: low iota (magenta line, label DAM), standard (blue lines, labels EIM and EJM), high mirror (green lines, label KKM), high iota (black lines, label FTM). The dashed red lines are exponential fits of the measurements. A prediction based on one-dimensional transport modelling and numerical calculation of the bootstrap current is shown in figure 5(b). The transport code requires as input the measured n_e and T_e profiles (not available for DAM). The time scale, mainly given by the R/L time ≈ 10 s (L and R are plasma inductance and resistance, respectively), and the expected strong reduction of the bootstrap current in high-mirror and high-iota configurations are well confirmed by both measurement and simulation. The simulations underestimate the measurements systematically (figure 5(b) solid lines). This might well be due to an (unintended) ECCD component, which is currently under investigation. By considering in the simulations reasonable residual ECCD of about 2–3 kA they quantitatively agree well with the measurements (figure 5(b) dashed lines). First findings on the reduction of the bootstrap current owing to magnetic field optimization were already reported from the previous operation campaign without divertor [19].

The long discharge duration enables to make use of electron cyclotron current drive (ECCD) for a feed-forward control of the (edge) rotational transform [27–29], which is changed by the toroidal current evolution that strongly depends on the magnetic configuration and the discharge parameters. Central co-/counter ECCD leads under certain discharge conditions to fast, repetitive electron temperature collapses in the core or even a total plasma collapse. This is likely due to the rotational transform crossing unity $\iota/2\pi = 1$, triggering an MHD instability [27, 29].

During the above discussed high density, high performance 1.1 MJ discharge with pellet injection into a helium target plasma (see section 3), electrons and ions thermalize and the ambipolar radial electric field E_r is expected to be negative throughout the plasma core (ion-root) [32]. This is clearly seen in measurements with the x-ray imaging crystal spectrometer (XICS, figure 6(a)), where the sudden transition from positive to negative E_r is correlated with the time interval

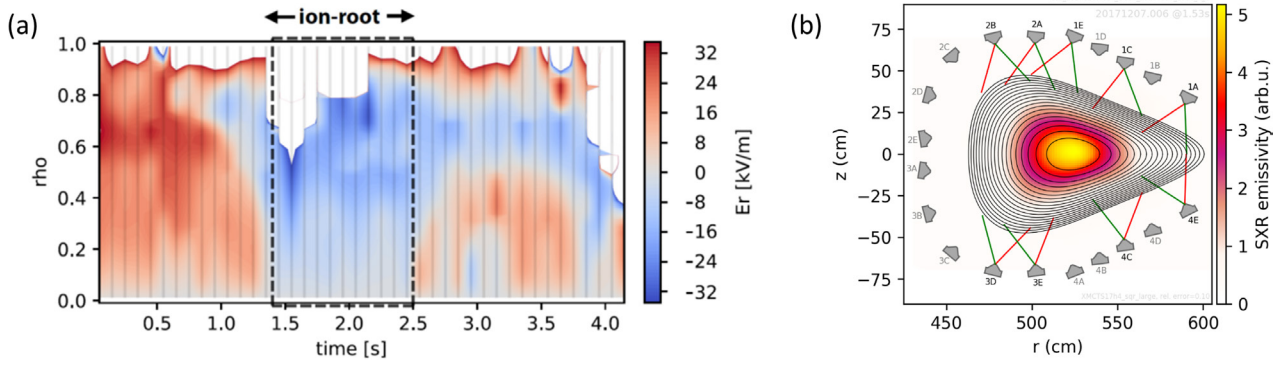


Figure 6. (a) Radial electric field measured with the x-ray imaging camera system. In the time interval $t = 1.5 \dots 2.5$ s a negative radial electric field forms throughout the entire plasma core. (b) Tomographic reconstruction of the soft x-ray radiation in the triangular plane, overlaid with the corresponding numerical plasma equilibrium calculation (VMEC). The x-ray cameras used for the reconstruction are indicated with their viewing lines.

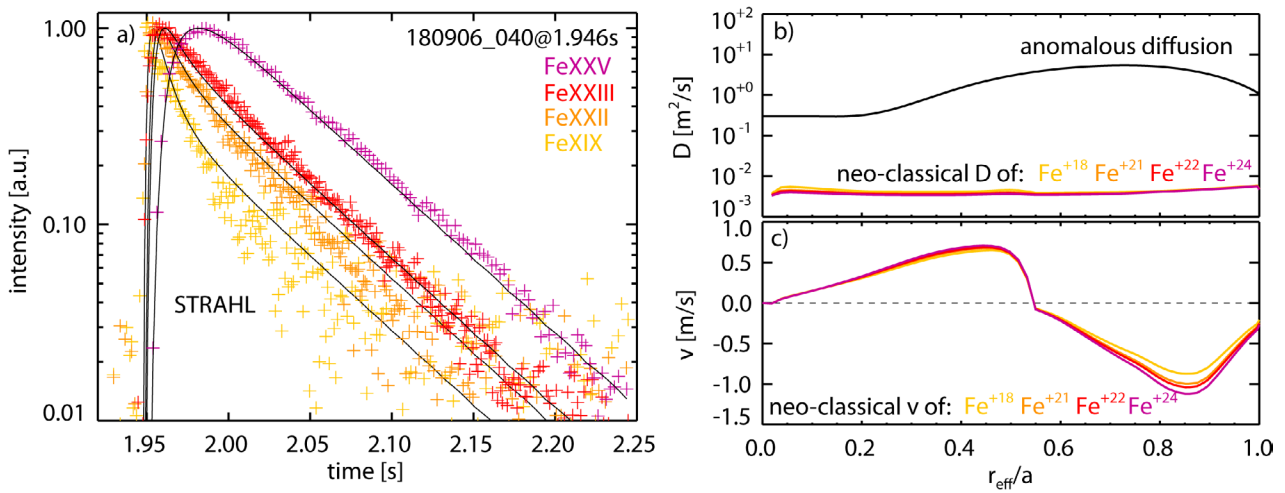


Figure 7. Laser blow-off injection of iron impurities into ECR heated hydrogen plasma. (a) Time evolution of selected iron ionization levels and forward-modelling curves (black lines). (b) Neoclassical and anomalous diffusion coefficient profiles. (c) Neoclassical convection velocity profiles.

during which $T_e \simeq T_i$. The neoclassical heat transport is predicted to be significantly reduced in the ion-root regime, as discussed more comprehensively in [34].

Figure 6(b) shows the tomographic reconstruction of the soft x-ray radiation at the triangular cross section, using a set of poloidally arranged x-ray cameras [35]. The measurement is overlaid with the numerically calculated plasma equilibrium using the VMEC code [36] for $\langle\beta\rangle = 1\%$. There is a good agreement between measured and calculated plasma equilibrium. The Shafranov shift is found to be 1–2 cm only, as predicted for the optimized stellarator magnetic field with reduced Pfirsch–Schlüter current. For $\langle\beta\rangle \leq 1.5\%$ the plasma in Wendelstein 7-X is expected to be MHD stable [3, 4] and indeed no distinct activity is observed in the magnetic and x-ray diagnostics. As mentioned above, MHD instabilities can be driven by central ECCD. Alfvén modes were observed under certain NBI discharge scenarios. The analysis of the corresponding data is in progress and will be published elsewhere.

Impurity transport is another key issue of (optimized) stellarators. As discussed in section 3 the radiative density

limit strongly depends on the impurity concentration fraction. Furthermore, impurity accumulation is considered as a major stellarator issue, since in particular in the ion-root confinement regime with $T_e \simeq T_i$, the neoclassical impurity convection is inwards-directed, as for example observed in the predecessor device Wendelstein 7-AS [37, 38]. Recent neoclassical transport investigations have demonstrated that temperature screening can arise in stellarator plasmas in a mixed collisionality regime (for hydrogen and impurity ions) at high ion temperatures [39]. Up to now, at $\langle\beta\rangle \leq 1.5\%$, in Wendelstein 7-X no evidence for impurity accumulation has been found in all relevant plasma scenarios, even at high particle densities in the $1 \times 10^{20} \text{ m}^{-3}$ range as well as in the ion-root confinement regime. To investigate the transport physics of impurity particles, active diagnostics namely laser blow-off (LBO) [40] and impurity pellet injection [41] (tracer encapsulated solid pellets, TESPEL) are used, combined with fast high-resolution spectrometers. Figure 7(a) shows the evolution of line radiation from different Fe ionization stages after injecting iron (LBO) into a hydrogen plasma at 5 MW of ECR heating power and a line-averaged plasma density of

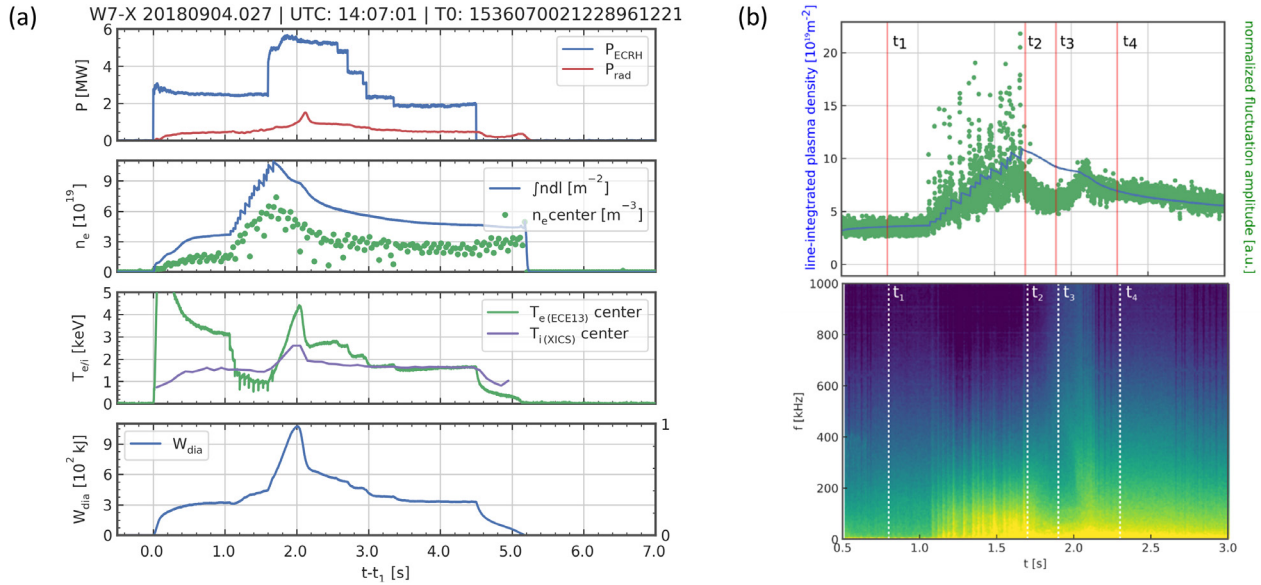


Figure 8. (a) High performance discharge with pellet injection during $t = 1 \dots 1.6$ s in a hydrogen target plasma. At $t = 1.6$ s the ECR heating power is doubled. The diamagnetic energy peaks at $t \approx 2$ s. (b) Temporal evolution of the line-integrated plasma density (blue) and the turbulent density fluctuation level (green) for a pellet-fueled discharge and the related spectrogram of plasma density fluctuations.

$2 \times 10^{19} \text{ m}^{-3}$. The rise-time and the decay-time of the different charge stages depend on the radial diffusion $D(r)$ and convection $v(r)$ profiles and consequently contain valuable information on the impurity transport. The measured data is compared with forward-modelling using the 1d impurity transport code STRAHL [42]. If as input parameters purely neo-classical diffusion and convection profiles are used, obtained from DKES [43] code runs (figures 7(b) and (c)), only poor agreement is obtained (not shown). In contrast to that, if additional anomalous diffusion is assumed (black line in figure 7(b)), the forward-modelling calculations match the experimental data very well (black curves in figure 7(a)). The corresponding level of anomalous diffusion is more than two orders of magnitude above the neo-classical level, which strongly suggests dominant turbulent transport. Probably ion temperature gradient (ITG) driven turbulence is the main contributor here, since ITG is expected during flat density gradients and high T_e/T_i ratios as present during the experiments [44]. More detailed and systematic studies under different plasma parameters, as well as comparisons with gyro-kinetic simulations, are ongoing [45].

Wendelstein 7-X is neoclassically optimized and turbulent transport is expected to play a significant role in the regulation of radial heat diffusivity and particle exhaust. Turbulence studies are therefore of key importance and a suite of diagnostic instruments is available, namely correlation reflectometry [18], various probes for edge turbulence measurements [46] and phase contrast imaging (PCI) for characterization of turbulence in the plasma core [47]. PCI samples plasma density fluctuations along the line-of-sight of an infrared laser beam in the predominantly unfavorable magnetic curvature region. Nonlinear gyrokinetic simulations indicate that ion temperature gradient (ITG) and trapped electron modes (TEM) are possible in the plasma core but the latter are different from their tokamak counterparts [48, 49]. Both modes

are unstable in regions of unfavorable magnetic curvature, which in Wendelstein 7-X are mainly localized in the out-board bean-shaped cross section. In usual gas-fueled discharges, ion temperature and plasma density gradient regions are well separated. Thus, ITG modes are destabilized deep in the plasma core, whereas TEM modes are localized in the edge plasma. An interesting observation is made with PCI when the plasma is centrally fueled by pellets (figure 8(a)). The density fluctuation amplitude is usually proportional to the line-integrated plasma density (figure 8(b)). However, after pellet fueling $t_2 = 1.6$ s, the fluctuation level suddenly drops and improved energy confinement is observed. The fluctuation spectrogram supports the picture: The entire fluctuation spectrum is temporarily reduced in amplitude, but evolves transiently for $t_3 < t < t_4$ starting from high frequencies until the usual linear scaling is recovered. Linear gyrokinetic simulations suggest [50], that the turbulence suppression is the result of a radial overlap between plasma density and temperature gradients, as it is generally observed in pellet discharges. Low T_e/T_i ratios and gradient length $L_{T_i} \simeq L_n \simeq 2\text{--}3\text{ m}$ stabilize ITG, whereas TEM is naturally stabilized by the good magnetic curvature regions [48, 49]. This observation shows that indeed turbulent transport plays an important role in Wendelstein 7-X and that its reduction, e.g. by centrally peaked density profiles, could well be the key for the development of improved confinement scenarios. A more comprehensive discussion of turbulence and the related transport is found in [51].

5. Summary





In conclusion the plasma performance of the optimized stellarator Wendelstein 7-X has significantly improved after the installation of the graphite island divertor and the graphite wall elements. Impurity and heat exhaust are now well under

control and long high-density discharges became accessible, especially after boronization. With a boronized wall, the radiative density limit could be shifted to three times higher values, on the expense of a slight degradation of the energy confinement time at the limit. With quite low ECR heating power, record values for the triple product in stellarators were achieved, albeit only transiently for a short time. The long discharges may well have set other records in comparison to other fusion research devices. The main limitations for high-performance long-pulse plasmas are limited heating power and not yet fully implemented water cooling of the in-vessel components. Nevertheless, in general excellent plasma performance with up to $\langle\beta\rangle = 1.2\%$ and $\beta(0) = 3.5\%$ was achieved by relatively modest ECR O-mode heating power. More heating power is needed to explore the high beta $\langle\beta\rangle > \leq 5\%$ and low $\nu^* = 10^{-6} \dots 10^{-5}$ regimes, where stellarator optimization is relevant in all aspects.

Acknowledgments

This work has been carried out within the framework of the EUROfusion Consortium and has received funding from the Euratom research and training program 2014–2018 and 2019–2020 under grant agreement No. 633053. The views and opinions expressed herein do not necessarily reflect those of the European Commission.

ORCID iDs

S. Bozhnikov  <https://orcid.org/0000-0003-4289-3532>
 B. Buttenschön  <https://orcid.org/0000-0002-9830-9641>
 N. Tamura  <https://orcid.org/0000-0003-1682-1519>
 T. Wegner  <https://orcid.org/0000-0003-0136-0406>

References

- [1] Boozer A. 2009 *Phys. Plasmas* **16** 058102
- [2] Nührenberg J. and Zille R. 1986 *Phys. Lett. A* **114** 129
- [3] Grieger G. et al 1992 *Phys. Fluids B* **4** 2081
- [4] Beidler C. et al 1990 *Fusion Sci. Technol.* **17** 148–68
- [5] Klinger T. et al 2017 *Plasma Phys. Control. Fusion* **59** 014018
- [6] Pedersen T.S. et al 2017 *Phys. Plasmas* **24** 055503
- [7] Wolf R.C. et al 2017 *Nucl. Fusion* **57** 102020
- [8] Klinger T. 2016 *Magnetic Fusion Energy: from Experiments to Power Plants* ed G. Neilson (Cambridge: Woodhead Publishing)
- [9] Klinger T. et al 2013 *Fusion Eng. Des.* **88** 461–5
- [10] Renner H. et al 2002 *Plasma Phys. Control. Fusion* **44** 1005–19
- [11] Bosch H.S. et al 2013 *Nucl. Fusion* **52** 126001
- [12] Nagel M. et al 2011 *Fusion Eng. Des.* **86** 1830–3
- [13] Erckmann V. et al 2007 *Fusion Sci. Technol.* **52** 291–312
- [14] Warmer F. et al 2016 *Plasma Phys. Control. Fusion* **58** 074006
- [15] McNeely P. et al 2013 *Fusion. Eng. Des.* **88** 1034–7
- [16] Ongena J. et al 2018 Preparing the ICRH system for the Wendelstein 7-X stellarator *Preprint: 2018 IAEA Fusion Energy Conf. (Gandhinagar, India, 22–27 October 2018)* EX/P8-27
- [17] Yokoyama M. et al 2007 *Nucl. Fusion* **47** 1213–9
- [18] Windisch T. et al 2017 *Plasma Phys. Control. Fusion* **59** 105002
- [19] Dinklage A. et al 2018 *Nat. Phys.* **14** 855–60
- [20] Wauters T. et al 2018 *Nucl. Fusion* **58** 066013
- [21] Bozhnikov S. et al 2018 High density and high performance operation with pellet injection in W7-X *Preprint: 2018 IAEA Fusion Energy Conf. (Gandhinagar, India, 22–27 October 2018)* EX/P8-8
- [22] Pedersen T.S. et al 2019 *Plasma Phys. Control. Fusion* **61** 014037
- [23] Brakel R. et al 2018 Strategy and optimization of wall conditioning at the Wendelstein 7-X stellarator *Preprint: 2018 IAEA Fusion Energy Conf. (Gandhinagar, India, 22–27 October 2018)* EX/P8-17
- [24] Fuchert G. et al 2018 Increasing the density in W7-X: benefits and limitations *Preprint: 2018 IAEA Fusion Energy Conf. (Gandhinagar, India, 22–27 October 2018)* EX/3-5
- [25] Zanca P. et al 2017 *Nucl. Fusion* **57** 056010
- [26] Winter J. et al 1990 *J. Nucl. Mater.* **14** 76–177
- [27] Wolf R. et al 2019 in preparation
- [28] Stange T. et al 2018 *Phys. Rev. Lett.* submitted
- [29] Laqua H.P. et al 2019 in preparation
- [30] Pedersen T.S. et al 2018 First divertor physics studies in Wendelstein 7-X *Preprint: 2018 IAEA Fusion Energy Conf. (Gandhinagar, India, 22–27 October 2018)* EX/9-1
- [31] Drevlak M. et al 2014 *Nucl. Fusion* **54** 073002
- [32] Helander P. et al 2012 *Plasma Phys. Control. Fusion* **54** 124009
- [33] Yamada H. et al 2005 *Nucl. Fusion* **45** 1684–93
- [34] Pablant N. et al 2018 Investigations of the role of neoclassical transport in ion-root plasmas on W7-X *Preprint: 2018 IAEA Fusion Energy Conf. (Gandhinagar, India, 22–27 October 2018)* EX/P8-31
- [35] Brandt C. et al 2017 *Fusion Eng. Design* **123** 887
- [36] Hirshman S.P. and Whitson J.C. 1983 *Phys. Fluids* **26** 3553
- [37] Giannone L. et al 2000 *Plasma Phys. Control. Fusion* **42** 603–27
- [38] Burhenn R. et al 2009 *Nucl. Fusion* **49** 065005
- [39] Helander P. et al 2017 *Phys. Rev. Lett.* **118** 155002
- [40] Wegner T. et al 2018 *Rev. Sci. Instrum.* **89** 073505
- [41] Bussiahn R. et al 2018 *Rev. Sci. Instrum.* **89** 10K112
- [42] Behringer K. et al 1987 *Plasma Phys. Fusion Technol.* **19** 57
- [43] Hirshman S.P. et al 1986 *Phys. Fluids* **29** 2951
- [44] Geiger B. et al 2019 *Nucl. Fusion* **59** 046009
- [45] Wegner T. et al 2019 in preparation
- [46] Killer C. et al 2018 Characterization of the W7-X scrape-off layer using the multipurpose manipulator *Preprint: 2018 IAEA Fusion Energy Conf. (Gandhinagar, India, 22–27 October 2018)* EX/P8-18
- [47] Edlund E. et al 2018 *Rev. Sci. Instrum.* **89** 10E105
- [48] Prohl J. et al 2013 *Phys. Rev. Lett.* **108** 245002
- [49] Plunk G. et al 2017 *J. Plasma Phys.* **83** 715830404
- [50] Alcuson J. et al 2019 in preparation
- [51] Grulke O. et al 2018 Plasma dynamics and transport studies in Wendelstein 7-X *Preprint: 2018 IAEA Fusion Energy Conf. (Gandhinagar, India, 22–27 October 2018)* EX/P8-9